ELSEVIER

# High resolution X-ray structure of potent anti-HIV pokeweed antiviral protein-III

Igor V. Kurinov[a,b], Fatih M. Uckun[a,c,*]

[a]*The Biotherapy and Drug Discovery Program, Parker Hughes Cancer Center, 2699 Patton Road, St. Paul, MN 55113, USA*
[b]*Department of Structural Biology, Parker Hughes Cancer Center, 2699 Patton Road, St. Paul, MN 55113, USA*
[c]*Department of Virology, Parker Hughes Cancer Center, 2699 Patton Road, St. Paul, MN 55113, USA*

## Abstract

Pokeweed antiviral protein III (PAP-III), a naturally occurring protein isolated from late summer leaves of the pokeweed plant (*Phytolacca americana*), has potent anti-HIV activity by an as yet undetermined molecular mechanism. PAP-III belongs to a family of ribosome-inactivating proteins that catalytically deadenylate ribosomal and viral RNA. The chemical modification of PAP-III by reductive methylation of its lysine residues significantly improved the crystal quality for X-ray diffraction studies. Trigonal crystals of the modified PAP-III, with unit cell parameters $a = b = 80.47$ Å, $c = 76.21$ Å, were obtained using 30% PEG400 as the precipitant. These crystals contained one enzyme molecule per asymmetric unit and diffracted up to 1.5 Å, when exposed to a synchrotron source. Here we report the X-ray crystal structure of PAP-III at 1.6 Å resolution, which was solved by molecular replacement using the homology model of PAP-III as a search model. The fold typical of other ribosome-inactivating proteins is conserved, despite several differences on the surface and in the loop regions. Residues Tyr[69], Tyr[117], Glu[172], and Arg[175] are expected to define the active site of PAP-III. Molecular modeling studies of the interactions of PAP-III and PAP-I with a single-stranded RNA heptamer predicted a more potent anti-HIV activity for PAP-III due to its unique surface topology and more favorable charge distribution in its 20 Å-long RNA binding active center cleft. In accordance with the predictions of the modeling studies, PAP-III was more potent than PAP-I in depurinating HIV-1 RNA.
© 2003 Elsevier Science Inc. All rights reserved.

*Keywords:* Pokeweed antiviral protein; X-ray structure; Ribosome inactivation; Anti-HIV protein

## 1. Introduction

PAP-III is a 30-kDa naturally occurring protein isolated from the late summer leaves of the pokeweed plant [1–3]. Several isoforms of PAP were isolated from spring leaves (PAP-I), early and late summer leaves (PAP-II and III), and seeds (PAP-S) of the pokeweed plant, and all PAPs have potent anti-HIV activity. The concentration of different PAP isoforms expressed in the pokeweed plant varies depending on environmental conditions such as water deficit. The structures of PAP-I and PAP-S have been described in detail [4–6]. The gene encoding PAP purified from summer leaves (originally called PAP-II) has been cloned and sequenced [7]. The primary structure of PAP from summer leaves is composed of 310 amino acids, and the final molecular weight of the mature protein is approximately 30 kDa. A comparison of the amino acid sequence of the PAP isoform from summer leaves with those of other RIPs revealed a moderate homology (42%) with PAP-I, and a lower homology (~20%) with ricin A-chain.

All PAPs belong to a family of RIPs, which catalytically remove a single adenine base from the highly conserved α-sarcin/ricin loop of ribosomal RNA. The ribosomes depurinated by PAP in this manner are unable to interact with the elongation factors (EF)-1 and EF-2, and thus protein synthesis is inhibited irreversibly at the translocation step [1,2,8,9]. PAP-I has been shown to effectively depurinate adenine-containing polynucleotides, single-stranded DNA, double-stranded DNA, and viral RNA [10–13], suggesting that the depurinating activity of PAP-I is not limited to the α-sarcin loop of rRNA. Recently, it was found that PAP-I can deguanylate both ribosomal and viral RNA [14,15]. Studies also indicated that PAPs effectively inhibit

intracellular replication of several animal viruses, including HIV [16–19]. It has been reported that several RIPs (momordica antiviral protein 30, gelonin, luffin, and saporin) inhibit the action of the viral integrase against the long terminal repeat (LTR) of HIV by binding to the LTR in competition with the viral integrase [20,21]. The molecular mechanism of the antiviral activity of PAPs is under active investigation [22–26] and has gained considerable interest in recent years due to the clinical use of native PAP as the active moiety of immunoconjugates against cancer and AIDS [27].

The PAP proteins from the pokeweed plant share a distinct but homologous primary structure. The putative active site residues participating in the rRNA depurination are highly conserved among the different PAP species. Furthermore, all three different PAP isoforms cause concentration-dependent depurination of genomic RNA purified from HIV-1 as well as bacteriophage MS2 RNA. All three PAP species are equally potent in inhibiting protein synthesis in a cell-free translation assay and in depurinating non-viral mouse RNA [13]. PAP-I, PAP-II, and PAP-III also inhibit the replication of HIV in human peripheral blood mononuclear cells at nanomolar concentrations [13].

We have determined the X-ray crystal structure of PAP-I at 2.0 Å resolution [5] and established a model of PAP/RNA interactions as a guide for the construction of superior PAP mutants [28]. However, our past efforts to crystallize PAP-III had not been successful. Here, we now report the successful crystallization of PAP-III after reductive methylation of its lysine residues and the high resolution X-ray structure of PAP-III, extended to a 1.6 Å resolution. The final structural model has an $R$-factor of 20.3% and a r.m.s.d. of 0.007 Å for bond lengths and 1.7° for angles. The primary fold typical for RIPs is conserved, despite many differences in the loop regions and surface topology, compared to that of PAP-I. The proteins from the RIP family usually differ from each other in the structure of their loops and surface topology, thus leading to different specificities and toxicity, which are important for the pharmaceutical application of these proteins. The structural comparison of PAP-III and PAP-I will likely provide further insights into the structure–activity relationships affecting their ribosome inactivation and antiviral properties.

In an attempt to evaluate the importance of the active site residues for the enzymatic deadenylation of ribosomal RNA and to improve our understanding of how PAP binds and depurinates viral RNA, we have also modeled the interaction of PAP-III with a single-stranded RNA heptamer, GAGAGGA. We have performed a comparative analysis with PAP-I to evaluate the importance of the different active site residues for the efficiency of enzymatic deadenylation of ribosomal and viral RNA. The structural insights gained from these analyses provide a cogent explanation for the previously reported experimental data showing that PAP-III is more effective than PAP-I in the deadenylation of viral RNA [13].

## 2. Materials and methods

### 2.1. Purification and chemical modification of PAP-III

PAP-III was extracted from late summer leaves of *Phytolacca americana* and purified to homogeneity as previously described [3,29]. During the elution by NaCl gradient, PAP-III elutes behind both PAP-I and PAP-II at a higher salt concentration. The PAP-III sample was a gift from Dr. J.D. Irvin (Southwest Texas State University). Just before the crystallization setup, PAP-III was repurified on a MonoS cation-exchange column (Pharmacia Biotech), eluted using 500 mM NaCl in 25 mM citric buffer, pH 6, and filtered through a 0.1 μm filter to remove possible aggregates.

Crystallization conditions were screened with the hanging-drop vapor-diffusion method at three different temperatures (4, 17, and 37°), initially using commercially available crystallization kits (Hampton Research). Very small and poorly shaped micro-crystals were found with PEG8000 as a precipitant and using extremely high protein concentrations of up to 140 mg/mL. All attempts to grow larger and better crystals failed without significant improvement of crystal quality, despite many trials with a large variety of crystallization conditions.

As reported in a few publications [30–32], the reductive methylation of lysine residues offers the opportunity to change the protein surface properties. It was also found that lysine modification with 2,4,6-trinitrobenzene sulfonyl chloride reduced the ability of PAP-I to inactivate ribosomes only slightly and had no detectable effect on its antiviral activity [33]. Because of the poor quality of the PAP-III crystals, the protein was subjected to reductive methylation of lysine residues to decrease its solubility and enhance its surface hydrophobicity, using the protocol published in Refs. [30,32]. In brief, the protein solution (∼10 mg/mL) was dialyzed against 0.2 M sodium borate, pH 8.5; 60 μL of formaldehyde (1 M) was added to 2 mL of the protein solution. Subsequently, 6 μL of sodium borohydrate (1 M) was added with rapid mixing, followed by the addition of another 4 μL of sodium borohydrate after 10 min. This modification reaction was repeated six times at 30-min intervals, during which the reaction solution was left on ice. The protein was concentrated and desalted by passage through a G-25 column previously equilibrated with water. The modified protein was then applied to a cation-exchange column and was eluted as a single peak at a lower NaCl concentration than unmodified wild-type PAP-III, indicating the reduced apparent surface charge.

### 2.2. Crystallization of reductively methylated PAP-III

The crystallization of modified PAP-III proved easier when compared to our years-long efforts to crystallize wild-type PAP-III protein. The crystals grew as thick

hexagonal rods from 30% PEG400 (pH 9.5–10) at 17° and ~15 mg/mL of protein solution. The crystals appeared after approximately 2–3 months and grew to maximum dimensions of approximately 0.3 mm × 0.3 mm × 0.7 mm within a half-year. For cryo-temperature data collection, the crystals were subjected to flash cooling in liquid nitrogen after a short (less than 5 sec) soaking in 50% PEG400 solution.

## 2.3. Data collection and processing

Initial X-ray diffraction data were collected using the R-AXIS IV imaging plate detector mounted on an RUH3R Rigaku rotating anode X-ray generator with a double mirror system operating at 50 kV and 100 mA. The crystal-to-detector distance was 125 mm, and the crystal in two different orientations was rotated around the spindle axis with images collected over 1.5° to a resolution of 2.3 Å. An X-ray data set was collected at low temperatures (~100 K) to improve the diffraction quality and to decrease the radiation decay.

A high-resolution full data set was collected at the Stanford Synchrotron Radiation Laboratory, using the crystallographic setup and accompanying support on beam-line BL7-1 at 0.97 Å wavelength. An MAR area detector system (345 mm) was used to collect data extending to 1.5 Å resolution at low temperature. The X-stream system from MSC was used for all low-temperature studies.

The diffraction data were evaluated using the HKL package [34]. The real resolution of the data, used for structure refinement, was estimated to be 1.6 Å by taking into consideration the completeness of the last resolution shell, $I/\sigma$ ratio and $R$-merge values. The completeness of the data set in the last resolution shell (1.66–1.60 Å) was 97.3%, and the $R$-merge factor was 13.2% (see Table 1 for full details).

PAP-III crystals belong to the primitive hexagonal lattice. The calculations of merging $R$-factors for various crystal symmetries led to the assignment of the $P321$ group. Examination of the systematic absences allowed

Table 1
Details of data collection and refinement

| | |
|---|---|
| Unit cell parameters (Å) | |
| $a$, $b$ | 80.47 |
| $c$ | 76.21 |
| $R$-merge (%) | 5.2 (13.2)[a] |
| % of Observed reflections with $I/\sigma > 1$ in the highest resolution bin | 97.3 |
| Resolution limit for refinement (Å) | 1.6 |
| Completeness of data used for refinement (%) | 97.1 |
| $R$-factor (%) | 20.3 |
| Number of water molecules | 260 |
| Protein main chain atoms $B$-factor (Å$^2$) | 11.5 |
| Protein side chain atoms $B$-factor (Å$^2$) | 14.2 |
| Water molecules $B$-factor (Å$^2$) | 26.8 |

[a] The number in parenthesis corresponds to the data in the highest resolution bin.

the identification of the space group $P3_121$ or $P3_221$ and the unit cell parameters $a = b = 80.47$ Å, $c = 76.21$ Å, $\alpha = \beta = 90°$, and $\gamma = 120°$. An acceptable crystal packing density $V_m$ of 2.30 Å$^3$/Da was calculated using the Matthews method [35], assuming the PAP-III crystals to contain one molecule per asymmetric unit. A total of 37,018 unique reflections were collected at the Stanford Synchrotron Radiation Laboratory, with a redundancy of 4.4. The data were first processed in the $P321$ group because of the ambiguous 3-fold axis. All structure refinement calculations were done using X-PLOR (version 3.8x) [36]; composite omit maps were calculated using CNS (version 1.0) [37].

## 2.4. Structure model refinement

We attempted structure solution using the molecular replacement method implemented in the programs X-PLOR/CNS [36,37] by employing our wild-type PAP-I model (PDB access code 1QCG) [5] as a search model. PAPs from spring and late summer leaves share only ~40% of identical residues, although there are many highly conserved residues and all RIPs with known structure possess a very similar folding pattern and structure. The only acceptable molecular replacement solution was found using the homology model of PAP-III, based on the sequence alignment with wild-type PAP-I. The modeling was done using the Homology module of *InsightII* [38]. The rotational search was followed by the Patterson correlation refinement and translational search implemented in CNS [37]. Rotational function searches were carried out with an integration radius of 25 Å. Although a prominent peak was found, all peaks of the rotational function search were used in the subsequent translation function search in two possible space groups, $P3_221$ and $P3_121$, followed by rigid-body refinement. The space group $P3_221$ was eliminated after several attempts revealed that it was impossible to have reasonable packing in a unit cell. The highest peak from the rotational search was 5.3$\sigma$ above the mean; the next highest peak was 4.6$\sigma$ above the mean. The highest peak from the translational function was 5.4$\sigma$ above the mean, and the next highest peak was only 4.8$\sigma$ above the mean. The most promising solution has an outstanding correlation peak and the lowest $R$-factor. The solution was examined graphically, and the crystal packing for this solution was good.

With the model given by molecular replacement, a rigid body refinement was carried out at 3.5 Å resolution. All data with $I/\sigma > 2$ and a low-resolution limit of 8 Å were used for structure refinement. Multiple cycles of slow-cooling annealing (5000 → 100 K), positional and restrained isotropic temperature factor refinements, were followed by visual inspection of the electron density maps, including omit maps, coupled with an intensive manual model re-building using the graphics program CHAIN [39]. Loops with residues inserted or deleted were adjusted

as polyalanines until side-chain electron density was apparent. Once a satisfactory description of the protein electron density was complete, water molecules were added based on the examination of an $F_o$–$F_c$ map. The water molecules with temperature factors higher than 55 Å$^2$ after each refinement step were deleted from the model. A total of 260 water molecules are included in the refined structure.

Strong stereochemical restraints were imposed during the crystallographic refinement, and the final PAP-III structure possessed a very good stereochemistry with a r.m.s.d. of 0.007 Å for bond lengths and 1.7° for angles. The r.m.s.d. between two molecules before and after the final round of refinement was less than 0.04 Å. The quality of the stereochemistry of the final protein structure was assessed with the PROCHECK package [40]. The Ramachandran plot showed 91.4% of all residues in the most favored regions and no residues in generously allowed or disallowed regions (data not shown). As a better guide to the quality of the structure, the values of the free *R*-factor were monitored during the course of the crystallographic refinement. The *R*-free factor (10% of the X-ray data was randomly omitted) was only 4% more than the conventional *R*-factor at the final stage of the structure refinement. Only at the last stage of the structure refinement were all data included in the calculations.

The refined coordinates of ligand-free PAP-III have been deposited in the Protein Data Bank (access code 1LLN).

## 2.5. Establishment of a theoretical model of a PAP-III complex with RNA

The depurination of ribosomes by PAPs occurs at a highly conserved stem-loop RNA structure, containing the GAGA motif. We, therefore, modeled the interaction of PAP-III with the single-stranded RNA heptamer GAGAGGA, to explore the mode of its interactions with viral RNA. The initial position of GAGAGGA single-stranded RNA was built manually, using RNA coordinates generated by *InsightII* [38]. The stretch of RNA was roughly positioned in the long concave region on the PAP-III surface, similar to our previous model of the PAP-I/RNA complex [28]. Subsequently, major steric collisions with the protein were removed by manually adjusting the torsion angles of the phosphate backbone. This general position of RNA was used as a starting point for subsequent docking trials. We created a definitive binding set of PAP-III residues in the active site cleft to move as a 3.5 Å shell around the manually docked ligand during the energy minimization. The rest of the protein molecule was fixed. The number of final docking positions was set to 10, although finally only 1–3 promising positions were identified. The calculations used a CVFF force-field in the *Discovery* program and a Monte Carlo strategy in the *Affinity* program. During the RNA docking, four torsion angles in the phosphate backbone near the bound alanine

were freed to increase the volume of conformational search. The parameters used in this docking included searching for five unique structures, 200 minimization steps for each structure, an energy range of 10.0 kcal/mol, maximum translation of the ligand of 1.5 Å, and maximum rotation of the ligand of 20°. The final binding position of the RNA heptamer was determined based on an evaluation of all favorable binding interactions, including contributions of the loss of translational and rotational entropy of the fragment, number and quality of hydrogen bonds, and contributions from ionic and lipophilic interactions to the binding energy.

## 3. Results and discussion

### 3.1. High resolution X-ray structure of PAP-III

Diffraction quality PAP-III crystals were obtained by the vapor diffusion method only after chemical modification of the lysine residues. The X-ray structure of PAP-III was solved by molecular replacement, using the homology model of PAP-III based on the sequence alignment with wild-type PAP-I, as a search model, and was refined at high resolution. The final PAP-III structural model included 260 water molecules and had an *R*-factor of 20.3% for all data between 8.0 and 1.6 Å resolution. The refined electron density clearly matched the published amino acid sequence of the PAP isoform from late summer leaves (amino acids 26–287) [7]. The detailed examination of the electron density implies that Ile-63 may be modeled as valine, Leu-130 as alanine, Val-167 as glycine, and Leu-254 as alanine. Several solvent-exposed amino acid residues not involved in the intermolecular contacts (mainly lysines) exhibited conformational disorder beyond the Cγ atom. No additional uninterpretable electron density was visible beyond both termini. Five amino acids from both the N- and the C-terminal were also confirmed by independent sequencing. The side chains of six amino acid residues were found to have alternative conformation. Unit cell parameters and details of data collection and refinement are summarized in Table 1.

A Cα trace superimposition of PAP-III with PAP-I is illustrated schematically in Fig. 1. The crystal structures of wild-type PAP-I and several other RIPs have been described in detail [4,5,41,42]. A direct comparison of the PAP-III structure with our published PAP-I structure (PDB code 1QCJ) shows a r.m.s.d. for the main chain atoms to be slightly more than 0.8 Å. A comparison of the residues in the active site region shows even less discrepancy with a r.m.s.d. of 0.5 Å. The largest deviations occur at external loops 103–111, 152–158, and 219–234; the last region includes a β-strand of the C-terminal region. We found that other residues that show large deviations between two PAP isoforms are either at external loops or on the surface of the protein.
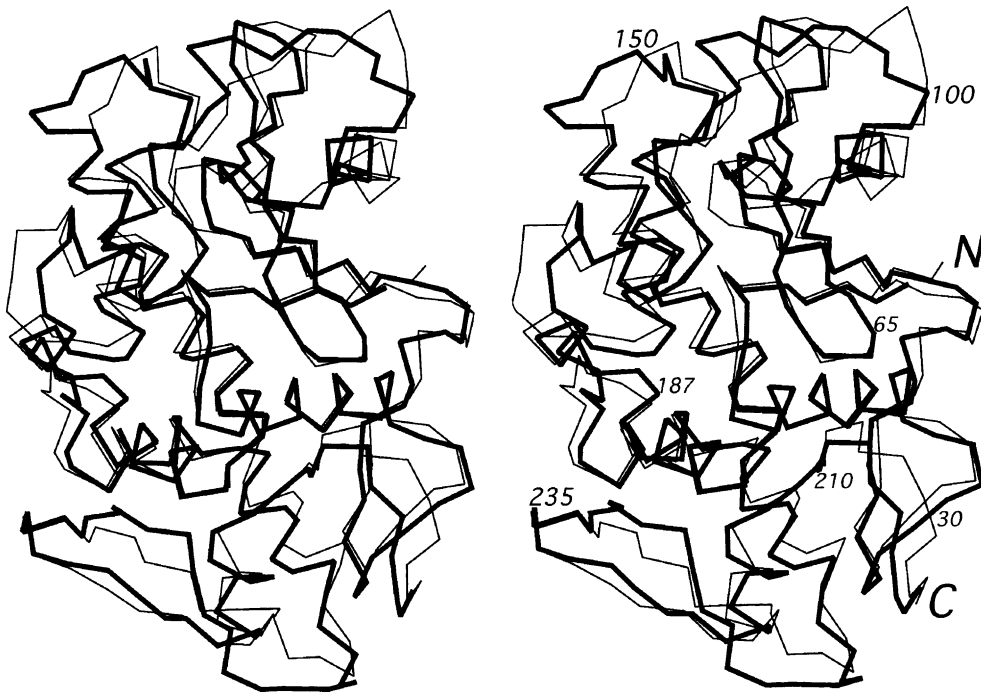
Fig. 1. A stereoscopic view of the Cα traces of PAP-III (thick line) and PAP-I (thin line) following superimposition of their respective main-chain coordinates. N- and C-termini are indicated. The overall folding and secondary structure patterns are very similar.

A ribbon diagram of the secondary structure of PAP-III is presented in Fig. 2. Despite their moderate sequence similarity (∼40%), PAP-III and PAP-I have very similar secondary structures. Analogous to other RIPs (ricin A-chain, trichosanthin, PAP-I), PAP-III is composed of two domains and has a well-defined secondary structure: eight α-helices and a twisted β-sheet composed of five strands (PAP-I has a six-stranded β-sheet). The well-conserved active site is located in the midsection of the long concave putative RNA-binding region and is enclosed mainly by α-helices. The overall fold of the protein is similar to other RIPs, but there are differences on the surface as well as in the loop regions. Insertions and deletions compared to PAP-I reside mainly in random coil regions. None of the
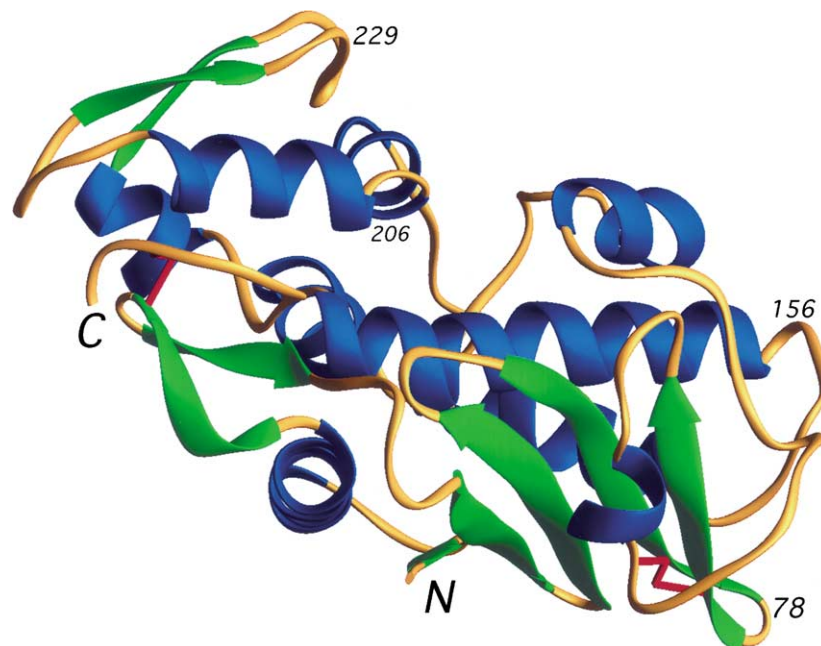


Fig. 2. The ribbon diagram of the PAP-III structural model. The active site of the proteins lies in the center between two domains. The two disulfides are shown in magenta. The diagram was created using RIBBONS software [43].
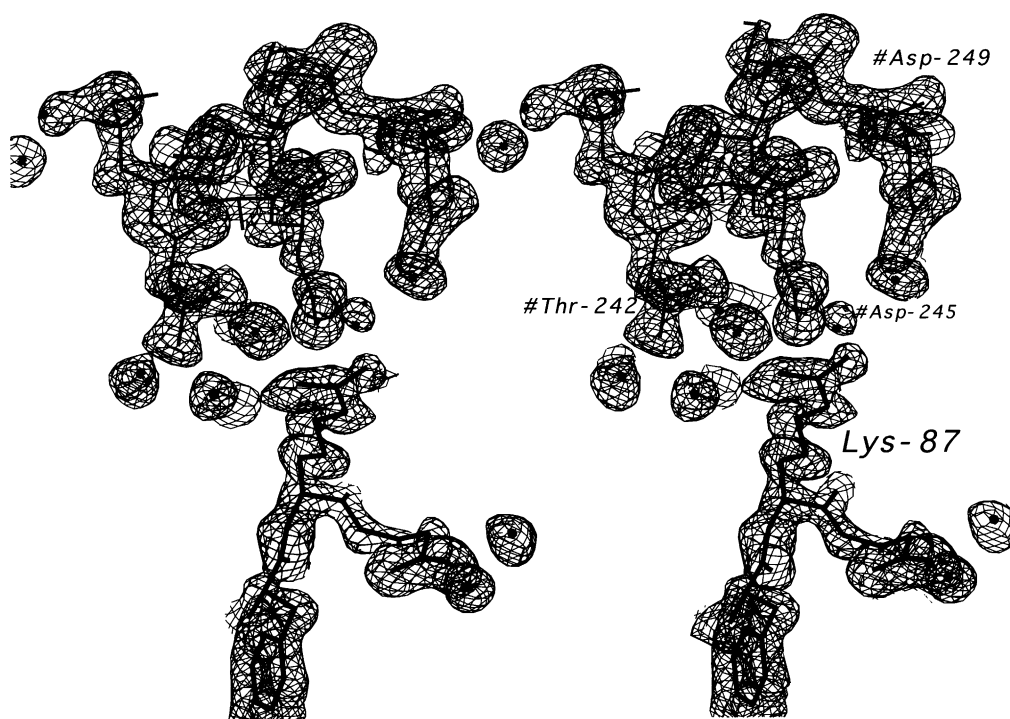
Fig. 3. The representative electron density for a section of the 1.6 Å composite omit $2F_o$–$F_c$ map [37] of the intermolecular contact involving methylated Lys-87 (thick line). The residues of the symmetry-related molecule are preceded by # (thin line). The map is contoured at $1.3\sigma$. The diagram was prepared using CHAIN [39].

insertions or deletions has a dramatic effect on the fold of the protein or affects the geometry of residues known to be involved in ribosome depurination. PAP-III contains two disulfide bonds, one between cysteines 32 and 259 and the other between residues 81 and 98.

For 14 well-ordered lysine residues we observed an additional electron density in the $F_o$–$F_c$ omit map by the end of side chains (Fig. 3). Thus, the principal product of the reductive methylation with formaldehyde appears to be ε-$N$,$N$-dimethyl lysine. From 32 lysine residues present in PAP-III, 10 lysines are involved directly in the intermolecular contacts (cutoff distance 4.0 Å). At least 5 lysines involved in the intermolecular contact have a dimethyl group clearly visible in the electron density. Thus, the protection of the positive charge of several lysines at the protein–protein interface by chemical modification is leading to the increase of favorable packing contacts between highly charged protein molecules, better crystal packing, and enhanced crystallization.

### 3.2. The enzymatic mechanism of PAP-III

Based on the crystal structures of ricin [41] and PAP-I [4] and mutagenesis studies [44], a distinct enzymatic reaction was proposed previously for the rRNA depurination by PAP-I which focuses on Glu[176] and Arg[179] (PAP-I numbering) as the central catalytic residues. The side chains of most of the active site residues of PAP-III (Tyr[69], Tyr[117], Glu[172], and Arg[175]) have roughly the same

positioning as the corresponding residues in PAP-I (Fig. 4). This active site structural similarity is consistent with the fact that PAP-III displays essentially the same enzymatic activity as PAP-I in a cell-free translation assay [13]. The following enzymatic mechanism can be suggested for PAP-III, based on the comparison with our PAP-I structure. After the adenine-containing substrate binds in the active site pocket by forming hydrogen bonds with the active site residues (Leu[70], Lys[115], and Arg[175]), the phenol ring of Tyr[69] rotates to reach nearly parallel and energy-favorable orientation with the target adenine base. The Arg[175] interacts with $N_3$ of the adenine base, possibly protonating it. The water molecules, preassociated with a $C'_1$–$N_9$ bond, nucleophilically attack $C'_1$, resulting in the cleavage of the $N$-glycosidic bond. This process is helped by the stabilization of the ribooxicarbonium-like transition state by the negatively charged side chain of Glu[172], which is close to $C'_1$. The examination of the crystal structure indicates that there are no other groups, which are closer to $N_7$ of the adenine base, capable of transferring a proton, as suggested for enzyme mechanism of trichosantin and momorcharin [42,45].

Although the central active site residues (Tyr[69], Tyr[117], Glu[172], Arg[175], and Trp[206]) are identical across the RIP family, adjacent residues involved in defining their positions do vary to some degree. It remains to be established what variability in catalytic constants, if any, may be related to these differences in the active site organization of RIPs. In spite of the strong conservation of the catalytic
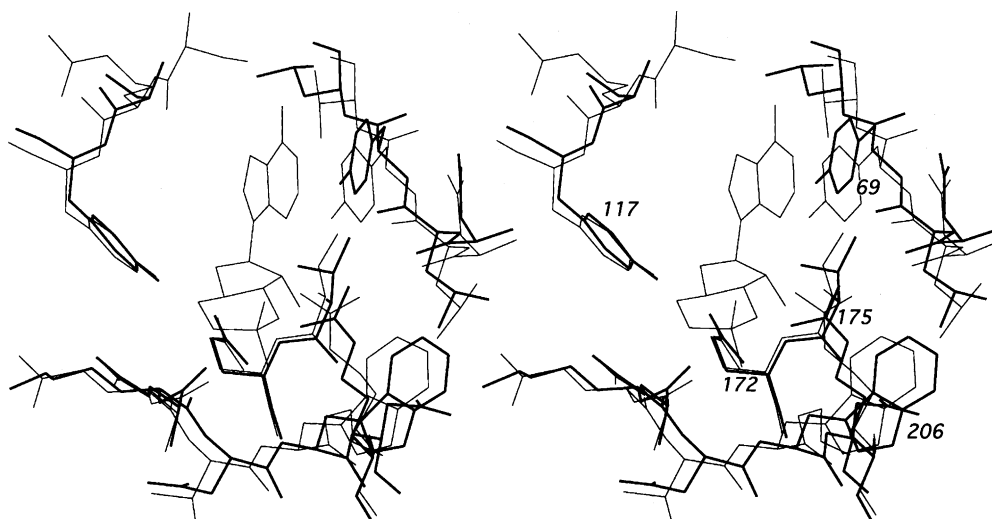
Fig. 4. Superimposition of the active site residues (PAP-III numbering) of PAP-III (thick line) and PAP-I (thin line). The model of PAP-I is shown with cyclic AMP strongly bound in the active site.

residues among members of the RIP family, these proteins differ significantly in substrate specificity and activity. Ricin A-chain, for example, does not depurinate the *Escherichia coli* ribosomes, whereas all PAPs do. Besides, the A-chain of ricin failed to cause detectable depurination of viral RNA, although it was almost as effective as PAP in ribosome depurination [13]. These findings indicate that the highly conserved active site residues responsible for the depurination of rRNA by PAPs or ricin are not sufficient for recognition and depurination of viral RNA. An experimentally obtained three-dimensional structure of PAP-III complexed with a larger substrate analogue consisting of a stem-loop structure may provide valuable information about the details of PAP-III specificity.

### 3.3. Modeling studies of the PAP-III interactions with RNA substrates

In an attempt to evaluate the importance of the active site residues for the enzymatic deadenylation of ribosomal RNA and improve our understanding of how PAP-III binds and depurinates ribosomal and viral RNA, we have modeled the interaction of PAP-III with a single-stranded RNA heptamer, GAGAGGA. Our model of a PAP-III complex with RNA (i.e. GAGAGGA complex) indicated that the target RNA heptamer can bind very strongly to PAP via multiple interactions along the long concave cleft region. The central adenine base is sandwiched between $Tyr^{69}$ and $Tyr^{117}$, as observed in a crystal structure, and forms three hydrogen bonds with active site residues ($Leu^{70}$, $Lys^{115}$, and $Arg^{175}$). There are many additional stabilizing electrostatic interactions between negatively charged phosphate groups and positively charged groups on the PAP-III surface formed by $Arg^{64}$ and $Lys^{211}$ from one side and by $Arg^{130}$, $Lys^{204}$, and $Lys^{231}$ from the other side of the active site. The two adjacent guanines (G-3 and G-5) of the bound

adenine (A-4) do not have any specific interactions with PAP-III, whereas the other ribonucleotides interact non-specifically with the active site cleft residues. These interactions help to properly position the adenine base in the PAP-III active site to be cleaved with high efficiency. The long binding cleft has the overall positive charge, favorable for binding the negatively charged phosphate backbone of RNA. The phosphate backbone of bound RNA adopts the conformation to avoid the negatively charged region. A comparison with the analogous PAP-I complex with RNA [28] shows that PAP-III has nearly the same mode of interaction as PAP in the closest vicinity of the active site, but differs at the distant sites of the binding cleft.

Fig. 5 illustrates the charge distribution and the surface topology of PAP-I and III structural models with bound RNA. When compared to PAP-III, PAP-I has no analogs to the positively charged $Lys^{185}$, $Lys^{189}$, and $Lys^{234}$ located on the RNA binding cleft. Moreover on a PAP-I surface, bound RNA has an additional unfavorable interaction with $Glu^{206}$ ($Lys^{207}$ in PAP-III). Obviously the removal of positively charged residues from the surface of the binding cleft will diminish the strength of binding to the negatively charged phosphate backbone of RNA and subsequently reduce the affinity of PAP-I toward the linear single-stranded RNA. It has been shown [13] that different PAP isoforms cause concentration-dependent depurination of genomic RNA purified from HIV-1 as well as bacteriophage MS2 RNA, and PAP-III has higher deadenylation efficiency than PAP-I. Therefore, our modeling studies provide a cogent explanation for experimentally documented higher depurination activity of single-stranded RNA (viral RNA) by PAP-III, as compared with PAP-I [13].

In summary, we have determined the high-resolution X-ray structure of PAP-III and gained insights into the structural basis of PAP-III interactions with RNA. Molecular modeling studies of the interactions of PAP-III with a
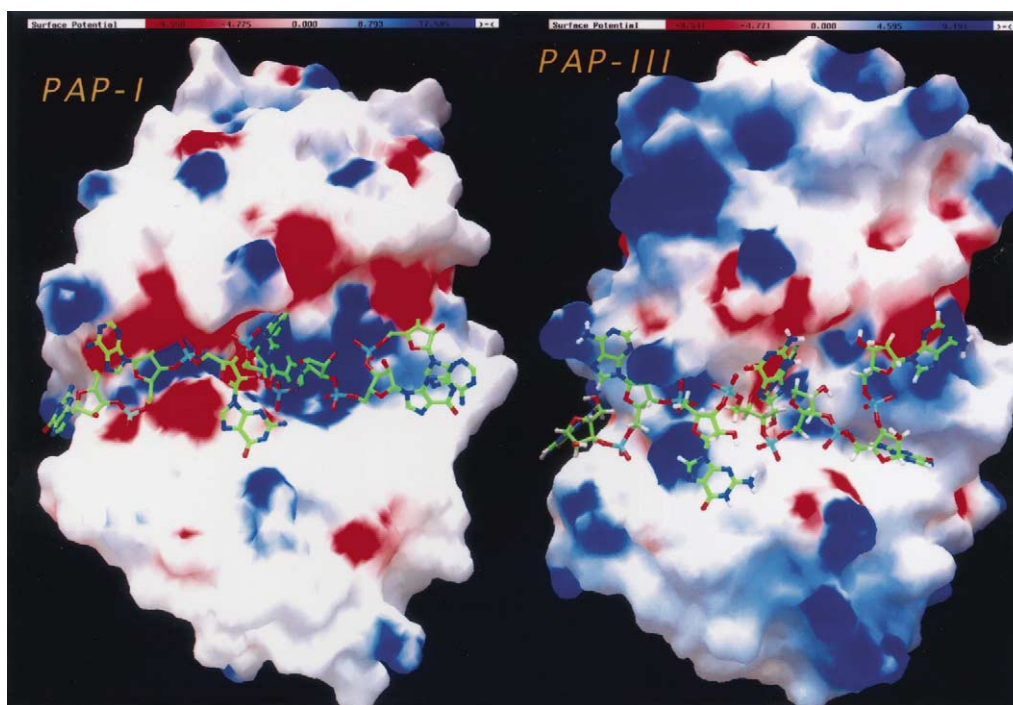
Fig. 5. Putative binding site of PAP-I (left) and PAP-III (right) for a single-stranded RNA (as a model of viral RNA). The analysis of the crystal structure revealed an active site pocket located in the midsection of the long concave binding region. The ball-and-stick model represents an RNA heptamer GAGAGGA that we docked into the binding site by computer simulation. The charge distribution on the PAP-III surface is different from PAP-I only at some distance from the active site pocket and explains the increased PAP-III affinity toward viral RNA. There are more positive (blue) patches on the PAP-III surface, as compared with PAP-I, near the bound RNA. The figure was created using GRASP software [46].

single-stranded RNA heptamer predicted a potent anti-HIV activity for PAP-III due to its unique surface topology and more favorable charge distribution in its 20 Å-long RNA binding active center cleft. In accordance with the predictions of the modeling studies, PAP-III depurinated HIV-1 RNA better than PAP-I [13]. The structural comparison of PAP-III and PAP-I will likely provide further insights into the structure–activity relationship, affecting their ribosome inactivating and antiviral properties.

## References

[1] Irvin JD. Pokeweed antiviral protein. Pharmacol Ther 1983;21: 371–87.

[2] Barbieri L, Batelli MG, Stirpe F. Ribosome-inactivating proteins from plants. Biochim Biophys Acta 1993;1154:237–82.

[3] Irvin JD, Kelly T, Robertus JD. Purification and properties of a second antiviral protein from *Phytolacca americana* which inactivates eukaryotic ribosomes. Arch Biochem Biophys 1980;200:418–25.

[4] Monzingo AF, Collins EJ, Ernst SR, Irvin JD, Robertus JD. The 2.5 Å structure of pokeweed antiviral protein. J Mol Biol 1993;233:705–15.

[5] Kurinov IV, Myers DE, Irvin JD, Uckun FM. X-ray crystallographic analysis of the structural basis for the interactions of pokeweed antiviral protein with its active site inhibitor and ribosomal RNA substrate analogs. Protein Sci 1999;8:1765–72.

[6] Li HM, Zeng ZH, Hu Z, Wang DC. Crystallization and preliminary crystallographic analyses of pokeweed antiviral protein from seeds. Acta Crystallogr D Biol Crystallogr 1998;54:137–9.

[7] Poyet JL, Radom J, Hoeveler A. Isolation and characterization of a cDNA clone encoding the pokeweed antiviral protein II from *Phytolacca americana* and its expression in *E. coli*. FEBS Lett 1994;347:268–72.

[8] Endo Y, Tsurugi K. The RNA *N*-glycosidase activity of ricin A-chain. The characteristics of the enzymatic activity of ricin A-chain with ribosomes and with rRNA. J Biol Chem 1988;263:8735–9.

[9] Gessner SL, Irvin JD. Inhibition of elongation factor 2-dependent translocation by the pokeweed antiviral protein and ricin. J Biol Chem 1980;255:3251–3.

[10] Barbieri L, Valbonesi P, Bonora E, Gorini P, Bolognesi A, Stirpe F. Polynucleotide:adenosine glycosidase activity of ribosome-inactivating proteins: effect on DNA RNA and poly(A). Nucleic Acids Res 1997;25:518–22.

[11] Nicolas E, Beggs JM, Haltiwanger BM, Taraschi TF. A new class of DNA glycosylase/apurinic/apyrimidinic lyases that act on specific adenines in single-stranded DNA. J Biol Chem 1988;273:17216–20.

[12] Wang P, Tumer NE. Pokeweed antiviral protein cleaves double-stranded supercoiled DNA using the same active site required to depurinate rRNA. Nucleic Acids Res 1999;27:1900–5.

[13] Rajamohan F, Venkatachalam TK, Irvin JD, Uckun FM. Pokeweed antiviral protein isoforms PAP-I, PAP-II, and PAP-III depurinate RNA of human immunodeficiency virus (HIV)-1. Biochem Biophys Res Commun 1999;260:453–8.

[14] Rajamohan F, Kurinov IV, Venkatachlam TK, Uckun FM. Deguanyla-tion of human immunodeficiency virus (HIV-1) RNA by recombinant pokeweed antiviral protein. Biochem Biophys Res Commun 1999; 263:419–24.

[15] Kurinov IV, Rajamohan F, Venkatachlam TK, Uckun FM. X-ray crystallographic analysis of the structural basis for the interaction of pokeweed antiviral protein with guanine residues of ribosomal RNA. Protein Sci 1999;8:2399–405.

[16] Aron GM, Irvin JD. Inhibition of herpes simplex virus multiplication by the pokeweed antiviral protein. Antimicrob Agents Chemother 1980;17:1032–3.

[17] Tomlinson JA, Walker VM, Flewett TH, Barclay GR. The inhibition of infection by cucumber mosaic virus and influenza virus by extracts from *Phytolacca americana*. J Gen Virol 1974;22:225–32.

[18] Gehrz RC, Wilson C, Eckhardt J, Myers DE, Irvin JD, Uckun FM. Treatment of human cytomegalovirus (HCMV) with noval antiviral immunoconjugates. In: Landini MP, editor. Progress in cytomegalovirus research. New York: Elsevier; 1991. p. 353–6.

[19] Zarling JM, Moran PA, Haffar O, Sias J, Richman DD, Spina CA, Myers DE, Kuebelbeck V, Ledbetter JA, Uckun FM. Inhibition of HIV replication by pokeweed antiviral protein targeted to CD4$^+$ cells by monoclonal antibodies. Nature 1990;347:92–5.

[20] Lee-Huang S, Huang PL, Huang PL, Bourinbaiar AS, Chen HC, Kung HF. Inhibition of the integrase of human immunodeficiency virus (HIV) type 1 by anti-HIV plant proteins MAP30 and GAP31. Proc Natl Acad Sci USA 1995;92:8818–22.

[21] Au TK, Collins RA, Lam TL, Ng TB, Fong WP, Wan DC. The plant ribosome inactivating proteins luffin and saporin are potent inhibitors of HIV-1 integrase. FEBS Lett 2000;471:169–72.

[22] Bonness MS, Ready MP, Irvin JD, Mabry TJ. Pokeweed antiviral protein inactivates pokeweed ribosomes implications for the antiviral mechanism. Plant J 1994;5:173–83.

[23] Chaddock JA, Lord JM, Hartley MR, Roberts LM. Pokeweed antiviral protein (PAP) mutations which permit *E. coli* growth do not eliminate catalytic activity towards prokaryotic ribosomes. Nucleic Acids Res 1994;22:1536–40.

[24] Hur Y, Hwang DJ, Zoubenko O, Coetzer C, Uckun FM, Tumer NE. Isolation and characterization of pokeweed antiviral protein mutations in *Saccharomyces cerevisiae*: identification of residues important for toxicity. Proc Natl Acad Sci USA 1995;92:8448–52.

[25] Tumer NE, Hwang DJ, Bonness M. C-terminal deletion mutant of pokeweed antiviral protein inhibits viral infection but does not depurinate host ribosomes. Proc Natl Acad Sci USA 1997;94:3866–71.

[26] Tumer NE, Parikh BA, Li P, Dinman JD. The pokeweed antiviral protein specifically inhibits Ty1-directed +1 ribosomal frameshifting and retrotransposition in *Saccharomyces cerevisiae*. J Virol 1998; 72:1036–42.

[27] Irvin JD, Uckun FM. Pokeweed antiviral protein: ribosome inactivation and therapeutic applications. Pharmacol Ther 1992;55:279–302.

[28] Rajamohan F, Pugmire MJ, Kurinov IV, Uckun FM. Modeling and alanine scanning mutagenesis studies of recombinant pokeweed antiviral protein. J Biol Chem 2000;275:3382–90.

[29] Myers DE, Irvin JD, Smith RS, Kuebelbeck VM, Uckun FM. Production of a pokeweed antiviral protein (PAP)-containing immunotoxin, B43-PAP, directed against the CD19 human B lineage lymphoid differentiation antigen in highly purified form for human clinical trials. J Immunol Methods 1991;136:221–37.

[30] Rypniewski WR, Holden HM, Rayment I. Structural consequences of reductive methylation of lysine residues in hen egg white lysozyme: an X-ray analysis at 1.8 Å resolution. Biochemistry 1993;32:9851–8.

[31] Means GE, Feeney RE. Reductive alkylation of amino groups in proteins. Biochemistry 1968;7:2192–201.

[32] Kurinov IV, Mao C, Irvin JD, Uckun FM. X-ray crystallographic analysis of pokeweed antiviral protein-II after reductive methylation of lysine residues. Biochem Biophys Res Commun 2000;275:549–52.

[33] Irvin JD, Aron GM. Chemical modifications of pokeweed antiviral protein: effects upon ribosome inactivation, antiviral activity and cytotoxicity. FEBS Lett 1982;148:127–30.

[34] Otwinnowski Z, Minor W. Processing of X-ray diffraction data collected in oscillation mode. Methods Enzymol 1997;276:307–25.

[35] Matthews BW. Solvent content of protein crystals. J Mol Biol 1968;33:491–7.

[36] Brunger AT. 1992 X-PLOR (version 3.1) Manual. New Haven, CT: Yale University Press; 1992.

[37] Brunger AT, Adams PD, Clore GM, DeLano WL, Gros P, Grosse-Kunstleve RW, Jiang JS, Kuszewski J, Nilges M, Pannu NS, Read RJ, Rice LM, Simonson T, Warren GL. Crystallography & NMR system: a new software suite for macromolecular structure determination. Acta Crystallogr D Biol Crystallogr 1998;54:905–21.

[38] InsightII. User guide. San Diego, CA: Molecular Simulations Inc.; 1991.

[39] Sack JS. CHAIN: a crystallographic modeling program. J Mol Graph 1988;6:224–5.

[40] Laskowski RA, MacArthur MW, Moss DS, Thornton JM. PROCHECK: a program to check the stereochemical quality of protein structures. J Appl Crystallogr 1993;26:283–91.

[41] Katzin BJ, Collins EJ, Robertus JD. Structure of ricin A-chain at 2.5 Å. Proteins 1991;10:251–9.

[42] Zhou K, Fu Z, Chen M, Lin Y, Pan K. Structure of trichosanthin at 1.88 Å resolution. Proteins 1994;19:4–13.

[43] Carson M. Ribbons Methods Enzymol 1997;277:493–505.

[44] Kim Y, Robertus JD. Analysis of several key active site residues of ricin A chain by mutagenesis and X-ray crystallography. Protein Eng 1992;5:775–9.

[45] Huang Q, Liu S, Tang Y, Jin S, Wang Y. Studies on crystal structures active-centre geometry and depurinating mechanism of two ribosome-inactivating proteins. Biochem J 1995;309:285–98.

[46] Nicholls A, Sharp KA, Honig B. Protein folding and association: insights from the interfacial and thermodynamic properties of hydrocarbons. Proteins 1991;11:281–96.